Research Article

Tower-Top Antenna Array Calibration Scheme for Next Generation Networks

Justine McCormack, Tim Cooper, and Ronan Farrell

*Centre for Telecommunications Value-Chain Research, Institute of Microelectronics and Wireless Systems,
National University of Ireland, Kildare, Ireland*

Recently, there has been increased interest in moving the RF electronics in basestations from the bottom of the tower to the top, yielding improved power efficiencies and reductions in infrastructural costs. Tower-top systems have faced resistance in the past due to such issues as increased weight, size, and poor potential reliability. However, modern advances in reducing the size and complexity of RF subsystems have made the tower-top model more viable. Tower-top relocation, however, faces many significant engineering challenges. Two such challenges are the calibration of the tower-top array and ensuring adequate reliability. We present a tower-top smart antenna calibration scheme designed for high-reliability tower-top operation. Our calibration scheme is based upon an array of coupled reference elements which sense the array's output. We outline the theoretical limits of the accuracy of this calibration, using simple feedback-based calibration algorithms, and present their predicted performance based on initial prototyping of a precision coupler circuit for a 2×2 array. As the basis for future study a more sophisticated algorithm for array calibration is also presented whose performance improves with array size.

1. INTRODUCTION

Antennas arrays have been commercially deployed in recent years in a range of applications such as mobile telephony, in order to provide directivity of coverage and increase system capacity. To achieve this, the gain and phase relationship between the elements of the antenna array must be known. Imbalances in these relationships can arise from thermal effects, antenna mutual coupling, component aging, and finite manufacturing tolerance [1]. To overcome these issues, calibration is required [2, 3]. Traditionally, calibration would have been undertaken at the manufacturer, address static effects arising from the manufacturing tolerances. However, imbalances due to dynamic effects require continual or dynamic calibration.

Array calibration of cellular systems has been the subject of much interest over the last decade (e.g., [4–6]), and although many calibration processes already exist, the issue of array calibration has, until now, been studied in a "tower-bottom" smart antenna context (e.g., tsunami(II) [2]). Industry acceptance of smart antennas has been slow, principally due to their expense, complexity, and stringent relia-

bility requirements. Therefore, alternative technologies have been used to increase network performance, such as cell splitting and tower-bottom hardware upgrades [7, 8].

To address the key impediments to industry acceptance of complexity and expense, we have been studying the feasibility of a self-contained, self-calibrating "tower-top" base transceiver station (BTS). This system sees the RF and mixed signal components of the base station relocated next to the antennas. This provides potential capital and operational savings from the perspective of the network operator due to the elimination of the feeder cables and machined duplexer filter. Furthermore, the self-contained calibration electronics simplify the issue of phasing the tower-top array from the perspective of the network provider.

Recent base station architectures have seen some departure from the conventional tower-bottom BTS and tower-top antenna model. First, amongst these was the deployment of tower-top duplexer low-noise amplifiers (TT-LNA), demonstrating a tacit willingness on the part of the network operator to relocate equipment to the tower-top if performance gains proved adequate and sufficient reliability could be achieved [9]. This willingness can be seen with the
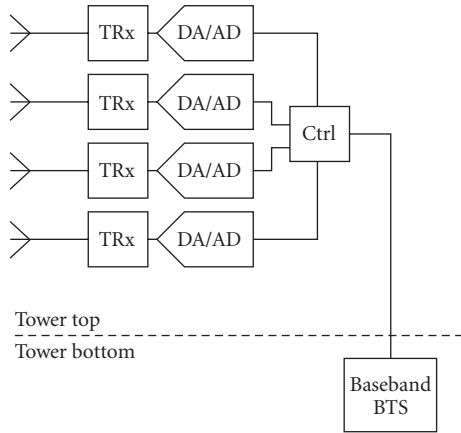
Figure 1: The hardware division between tower top and bottom for the tower-top BTS.

Figure 2: A simplified block schematic diagram of a typical array calibration system.

exploration of novel basestation architectures, with examples such as reduced RF feeder structures utilising novel switching methodologies [10, 11], and the development of basestation hotelling with remote RF heads [12]. Such approaches aim to reduce capital infrastructure costs, and also site rental or acquisition costs [13].

In this paper, we present our progress toward a reliable, self-contained, low-cost calibration system for a tower-top cellular BTS. The paper initially presents a novel scheme for the calibration of an arbitray-sized rectilinear array using a structure of interlaced reference elements. This is followed in Section 3 by a theoretical analysis of this scheme and predicted performance. Section 4 presents a description of a prototype implementation with a comparison between experimental and predicted performance. Section 5 presents some alternative calibration approaches utilising the same physical structure.

2.   RECTILINEAR ARRAY CALIBRATION

2.1.   Array calibration

To yield a cost-effective solution for the cellular BTS market, we have been studying the tower-top transceiver configuration shown in Figure 1. This configuration has numerous advantages over the tower-bottom system but, most notably, considerably lower hardware cost than a conventional tower-bottom BTS may be achieved [14].

We define two varieties of array calibration. The first, radiative calibration, employs free space as the calibration path between antennas. The second, where calibration is performed by means of a wired or transmission line path and any radiation from the array in the process of calibration is ancillary, is refered to as "nonradiative" calibration. The setup of Figure 2 is typically of a nonradiative calibration process [2]. This process is based upon a closed feedback loop between the radiative elements of the array and a sensor. This sensor provides error information on the array output and generates an error signal. This error signal is fed back to correctively weight the array element's input (transmit cal-
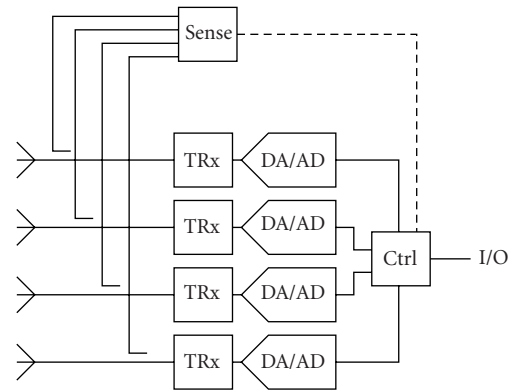
ibration) or output (receive calibration). It is important to observe that this method of calibration does not correct for errors induced by antenna mutual coupling. Note that in our calibration scheme, a twofold approach will be taken to compensate for mutual coupling. The first is to minimise mutual coupling by screening neighbouring antennas—and perhaps using electromagnetic (EM) bandgap materials to reduce surface wave propagation to distant antennas in large arrays. The second is the use of EM modelling-based mitigation such as that demonstrated by Dandekar et al. [6]. Further discussion of mutual coupling compensation is beyond the scope of this paper.

While wideband calibration is of increasing interest, it remains difficult to implement. On the other hand, narrowband calibration schemes are more likely to be practically implemented [1]. The calibration approach presented here is directed towards narrowband calibration. However, the methodology supports wideband calibration through sampling at different frequencies.

2.2.   Calibration of a 2×2 array

Our calibration process employs the same nonradiative calibration principle as shown in Figure 2. The basic building block, however, upon which our calibration system is based is shown in Figure 3. This features four radiative array transceiver elements, each of which is coupled by transmission line to a central, nonradiative reference element.

In the case of transmit calibration (although by reciprocity receive calibration is also possible), the transmit signal is sent as a digital baseband signal to the tower-top and is split (individually addressed) to each transmitter for SISO (MIMO) operation. This functionality is subsumed into the control (Ctrl) unit of Figure 3.

Remaining with our transmit calibration example, the reference element sequentially receives the signals in turn from the feed point of each of the radiative array elements. This enables the measurement of their phase and amplitude relative to some reference signal. This information on the
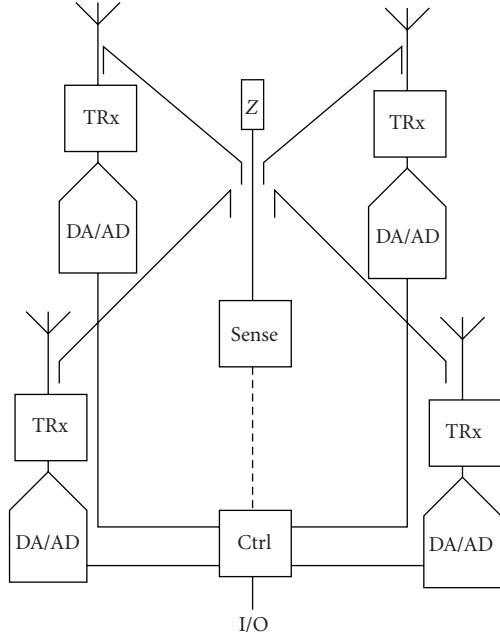
FIGURE 3: A central, nonradiative reference sensor element coupled to four radiative array transceiver elements.
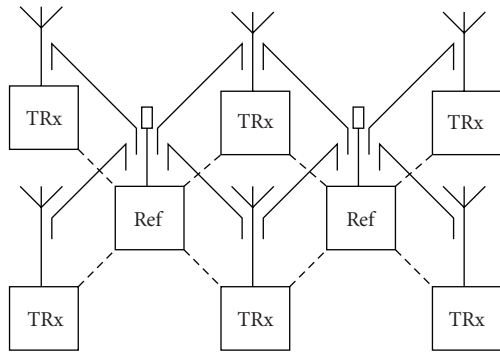

FIGURE 4: A pair of reference elements, used to calibrate a 2×3 array.

relative phase and amplitude imbalance between the feed points of each of the transceivers is used to create an error signal. This error signal is fed back and used to weight the input signal to the transceiver element—effecting calibration. Repeating this procedure for the two remaining elements calibrates our simple 2×2 array. This baseband feedback system is to be implemented in the digital domain, at the tower-top. The functionality of this system and the attendant computing power, energy, and cost requirements of this system are currently under investigation.

2.3. Calibration of an $n \times n$ array

By repeating this basic 2×2 pattern with a central reference element, it becomes possible to calibrate larger arrays [15]. Figure 4 shows the extension of this basic calibration principle to a 2×3 array.
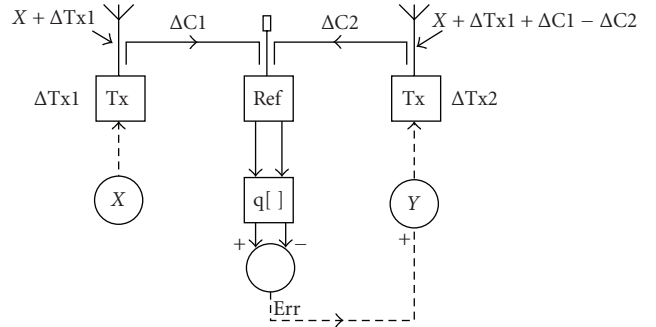

FIGURE 5: Propagation of error between calibrating elements.

To calibrate a large, $n \times n$, antenna array, it is easy to see how this tessellation of array transceivers and reference elements could be extended arbitrarily to make any rectilinear array geometry.

From the perspective of a conventional array, this has the effect of interleaving a second array of reference sensor elements between the lines of radiative transceiver elements, herein referred to as "interlinear" reference elements, to perform calibration. Each reference is coupled to four adjacent radiative antenna elements via the six-port transmission line structure as before. Importantly, because there are reference elements shared by multiple radiative transceiver elements, a sequence must be imposed on the calibration process. Thus, each transceiver must be calibrated relative to those already characterised.

Cursorily, this increase in hardware at the tower-top due to our interlinear reference elements has the deleterious effect of increasing the cost, weight, and power inefficiency of the radio system. The reference element hardware overhead, however, produces three important benefits in a tower-top system: (i) many shared reference elements will enhance the reliability of the calibration scheme—a critical parameter for a tower-top array; (ii) the array design is inherently scalable to large, arbitrary shape, planar array geometries; (iii) as we will show later in this paper, whilst these reference nodes are functional, the multiple calibration paths between them may potentially be used to improve the calibration accuracy of the array. For now, however, we consider basic calibration based on a closed loop feedback mechanism.

3. RECTILINEAR CALIBRATION—THEORY OF OPERATION

3.1. Basic calibration

Figure 5 shows a portion of an $n \times n$ array where two of the radiative elements of our array are coupled to a central reference transceiver. As detailed in Section 2.2, the calibration begins by comparing the output of transceiver 1 with transceiver 2, via the coupled interlinear reference element. Assuming phase only calibration of a SISO system, at a single frequency and with perfect impedance matching, each of the arbitrary phase errors incured on the signals, that are sent through the calibration system, may be considered additive

constants (Δi, where i is the system element in question). Where there is no variation between the coupled paths and the accuracy of the phase measurement process is arbitrarily high, then, as can be seen in Figure 5, the calibration process is essentially perfect.

However, due to finite measurement accuracy and coupler balance, errors propagate through the calibration scheme. Initial sensitivity analysis [16] showed that when the resolution of the measurement accuracy, q[ ], is greater than or equal to 14 bits (such as that attainable using modern DDS, e.g., AD9954 [17] for phase control), the dominant source of error is the coupler imbalance.

From Figure 5 it is clear that an error, equal in magnitude to the pair of coupler imbalances that the calibration signal encounters, is passed on to the feed point of each calibrated transceiver. If this second transceiver is then used in subsequent calibration operations, this error is passed on. Clearly, this cumulative calibration error is proportional to the number of the calibration couplers in a given calibration path. For simple calibration algorithms such as that shown in Figure 5, the array geometry and calibration path limit the accuracy with which the array may be calibrated.

3.2. Theoretical calibration accuracy

3.2.1. Linear array

Figure 6(a) shows the hypothetical calibration path taken in phasing a linear array of antennas. Each square represents a radiative array element. Each number denotes the number of coupled calibration paths accrued in the calibration of that element, relative to the first element numbered 0 (here the centremost). If we choose to model the phase and amplitude imbalance of the coupler (σ_{c_k}) as identically distributed Gaussian, independent random variables, then the accuracy of calibration for the linear array of N elements relative to the centre element, σ_{a_k}, will be given by the following:

even N:

$$\sigma_{a_k}^2 = \frac{2\sigma_{c_k}^2}{N-1} \sum_{i=1}^{N/2} 2i, \tag{1}$$

odd N:

$$\sigma_{a_k}^2 = \frac{2\sigma_{c_k}^2}{N-1} \left(\left[\sum_{i=1}^{N/2} 2i \right] + 1 \right), \tag{2}$$

where the subscript $k = A$ or ϕ for amplitude or phase error. With this calibration topology, linear arrays are the hardest to accurately phase as they encounter the highest cumulative error. This can be mitigated in part (as shown here) by starting the calibration at the centre of the array.

3.2.2. Square array

Based on this observation, a superior array geometry for this calibration scheme is a square. Two example square arrays calibration methods are shown in Figures 6(b) and 6(c). The former initiates calibration relative to the top-left hand
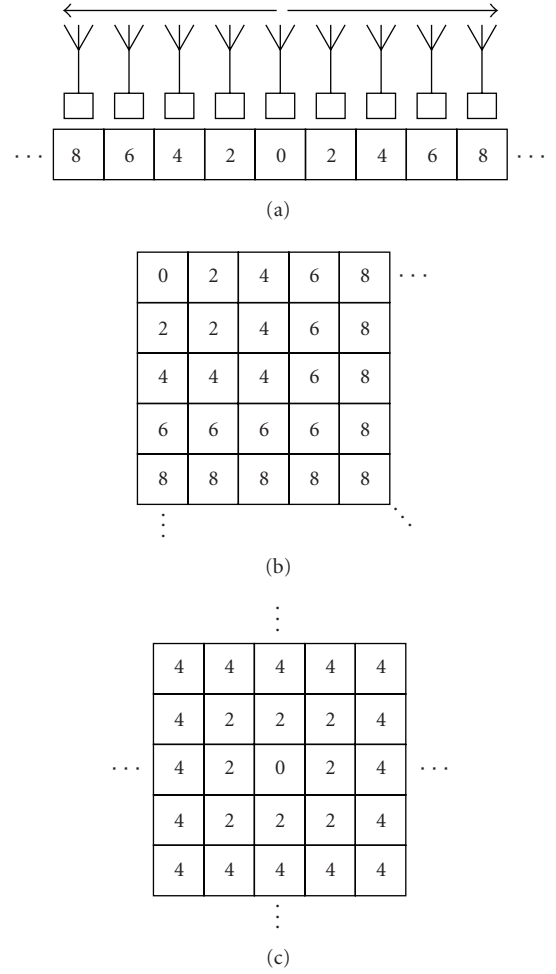

FIGURE 6: Calibration paths through (a) the linear array. Also the square array starting from (b) the top left and (c) the centre of the array.

transceiver element. The calibration path then propagates down through to the rest of the array taking the shortest path possible. Based upon the preceding analysis, the predicted calibration accuracy due to coupler imbalance of an $n \times n$ array is given by

$$\sigma_{a_k}^2 = \frac{2\sigma_{c_k}^2}{N-1} \sum_{i=1}^{n} (2i-1)(i-1) \tag{3}$$

with coupler error variance $\sigma_{c_k}^2$, centred around a mean equal to the value of the first element.

Figure 6(c) shows the optimal calibration path for a square array, starting at the centre and then radiating to the periphery of the array by the shortest path possible. The closed form expressions for predicting the overall calibration accuracy of the array relative to element 0 are most conveniently expressed for the odd and even n, where $n^2 = N$:

even n:

$$\sigma_{a_k}^2 = \frac{2\sigma_{c_k}^2}{N-1} \left(\left[\sum_{i=1}^{n/2-1} (8i)(2i) \right] \right) + \frac{2n-1}{N-1} n\sigma_{c_k}^2, \tag{4}$$

TABLE 1

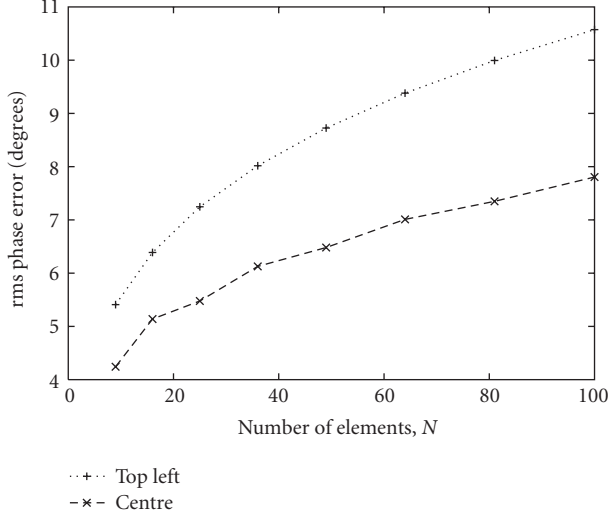| Component (i)	μ_{i_A}	σ_{i_A}	μ_{i_ϕ}	σ_{i_ϕ}
Tx S_{21}	50 dB	3 dB	10°	20°
Ref S_{21}	60 dB	3 dB	85°	20°
Cal S_{21}	−40 dB	0.1 dB	95°	3°

FIGURE 7: Comparison of the theoretical phase accuracy predicted by the closed form expressions for the square array calibration schemes, with $\sigma_{c_\phi} = 3°$.
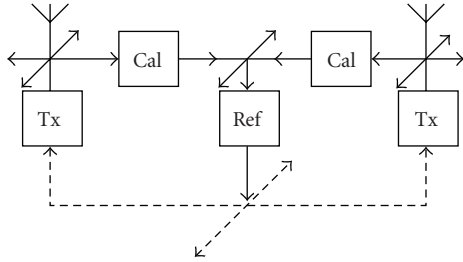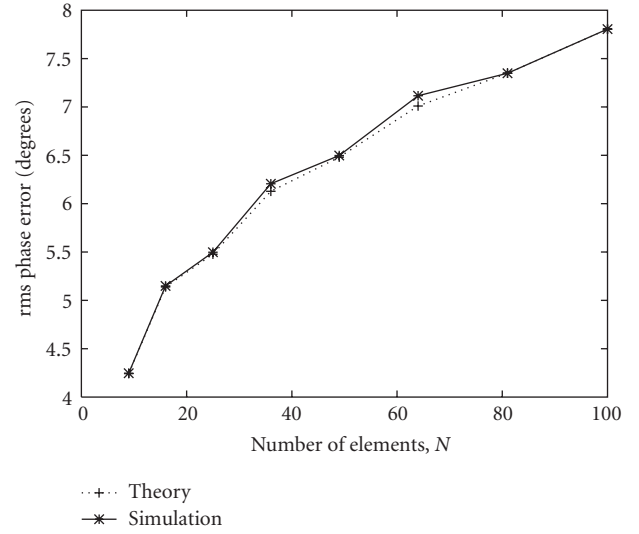

FIGURE 9: The overall array calibration accuracy predicted by (4) and the calibration simulation for $\sigma_{c_\phi} = 3°$.

FIGURE 8: Block schematic diagram of the array calibration simulation used to test the accuracy of the theoretical predictions.

3.3. Simulation

3.3.1. Calibration simulation system

To determine the accuracy of our theoretical predictions on array calibration, a simulation comprising the system shown in Figure 8 was implemented. This simulation was based on the S-parameters of each block of the system, again assuming perfect impedance matching and infinite measurement resolution. Attributed to each block of this schematic was a mean performance (μ_{i_k}) and a normally distributed rms error (σ_{i_k}), which are shown in Table 1.

odd n:

$$\sigma_{a_k}^2 = \frac{2\sigma_{c_k}^2}{N-1} \sum_{i=1}^{n/2-1/2} (8i)(2i). \tag{5}$$

A graph of the relative performance of each of these two calibration paths as a function of array size (for square arrays only) is shown in Figure 7. This shows, as predicted, that the phasing error increases with array size. The effect of this error accumulation is reduced when the number of coupler errors accrued in that calibration is lower—that is, when the calibration path is shorter. Hence, the performance of the centre calibrated array is superior and does not degrade as severely as the top-left calibrated array for large array sizes.

As array sizes increase, the calibration path lengths will inherently increase. This will mean that the outer elements will tend to have a greater error compared to those near the reference element. While this will have impact on the array performance, for example, in beamforming, it is difficult to quantify. However, in a large array the impact of a small number of elements with relatively large errors is reduced.

3.3.2. Results

For each of the square array sizes, the results of 10 000 simulations were complied to obtain a statistically significant sample of results. For brevity and clarity, only the phase results for the centre-referenced calibration are shown, although comparable accuracy was also attained for both the amplitude output and the "top-left" algorithm. Figure 9 shows the phase accuracy of the centre-referenced calibration algorithm. Here we can see good agreement between theory and simulation. The reason for the fluctuation in both the theoretical and simulated values is because of the difference between the even and odd n predictions for the array accuracy. This difference arises because even n arrays do not have a centre element, thus the periphery of the array farthest from the nominated centre element incurs slightly higher error.
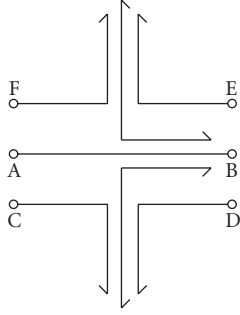
FIGURE 10: Schematic representation of the six-port, precision directional coupler.

3.3.3. Practical calibration accuracy

These calibration schemes are only useful if they can calibrate the array to within the limits useful for adaptive beamforming. The principle criterion on which this usefulness is based is on meeting the specifications of 1 dB peak amplitude error and 5° rms phase error [16]. The preceding analysis has shown that, in the absence of measurement error,

$$\lim_{\sigma_c \to 0} \sigma_a \longrightarrow 0, \qquad (6)$$

where σ_a is the rms error of the overall array calibration error. Because of this, limiting the dominant source of phase and amplitude imbalance, that of the array feed-point coupler structure, will directly improve the accuracy of the array calibration.

4. THE CALIBRATION COUPLER

4.1. 2×2 array calibration coupler

The phase and amplitude balance of the six-port coupler structure at the feed point of every transceiver and reference element in Figure 4 is crucial to the performance of our calibration scheme. This six-port coupler structure is shown schematically in Figure 10. In the case of the reference element, the output (port B) is terminated in a matched load (antenna) and the input connected to the reference element hardware (port A). Ports C–F of the coupler feed adjacent transceiver or reference elements. Similarly, for the radiative transceiver element, port B is connected to the antenna element and port A the transceiver RF hardware. For the individual coupler shown in Figure 10 using conventional low-cost, stripline, board fabrication techniques, phase balance of 0.2 dB and 0.9° is possible [18]. By interconnecting five of these couplers, then the basic 2×2 array plus single reference sensor element building block of our scheme is formed. It is this pair of precision six-port directional couplers whose combined error will form the individual calibration paths between transceiver and reference element.

A schematic representation of the 2×2 array coupler is shown in Figure 11. This forms the feed-point coupler structure of Figure 4, with the central coupler (port 1) connected to the reference element and the load (port 2). Each peripheral couplers is connected to a radiative transceiver element
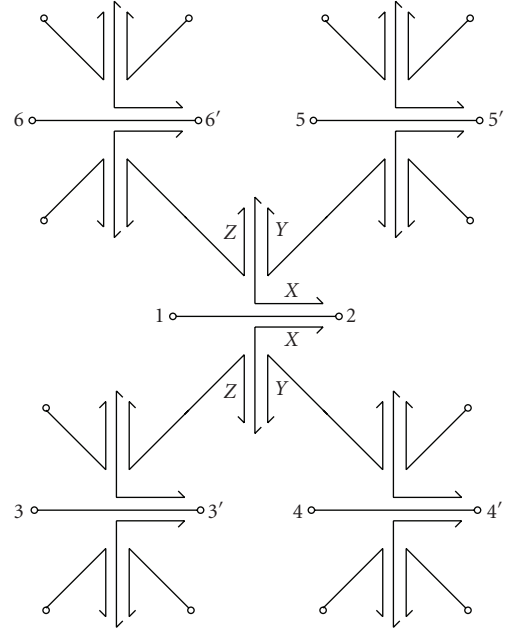

FIGURE 11: Five precision couplers configured for 2×2 array calibration.

(ports 3–6). By tiling identical couplers at half integer wavelength spacing, our objective was to produce a coupler network with very high phase and amplitude balance.

4.2. Theoretical coupler performance

The simulation results for our coupler design, using ADS momentum, are shown in Figure 12 [19]. Insertion loss at the design frequency of 2.46 GHz is predicted as 0.7 dB. The intertransceiver isolation is high—a minimum of 70.4 dB between transceivers. In the design of the coupler structure, a tradeoff exists between insertion loss and transceiver isolation. By reducing the coupling factor between the antenna feeder transmission line and the coupled calibration path (marked X on Figure 11), higher efficiency may be attained. However, weaker calibration coupling than −40 dBm is undesirable from the perspective of calibration reference element efficiency and measurement reliability. This necessitates stronger coupling between the calibration couplers—this stronger coupling in the second coupler stage (marked Y or Z on Figure 11) will reduce transceiver isolation. It is for this reason that −20 dB couplers are employed in all instances (X, Y, and Z).

The ADS simulation predicts that the calibration path will exhibit a coupling factor of −44.4 dB, slightly higher than desired.

The phase and amplitude balance predicted by the simulation is shown in Figures 13 and 14. This is lower than reported for a single coupler. This is because the individual coupler exhibits a natural bias toward high phase balance between the symmetrical pairs of coupled lines—ports D,E and C,F of Figure 10. In placing the couplers as shown in Figure 11, the error in the coupled path sees the sum of an
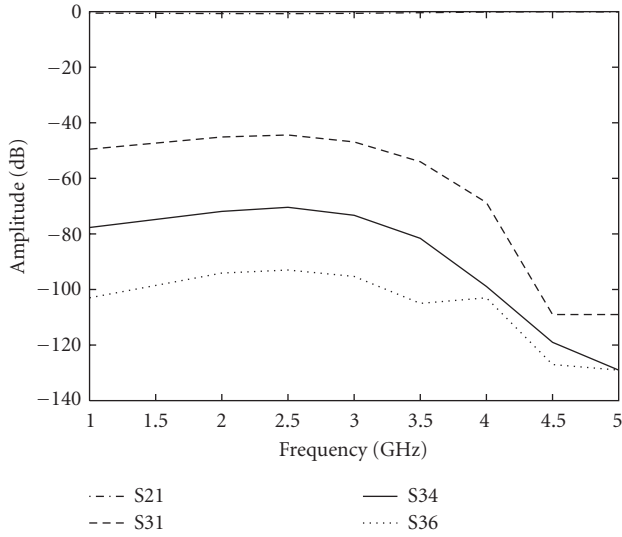
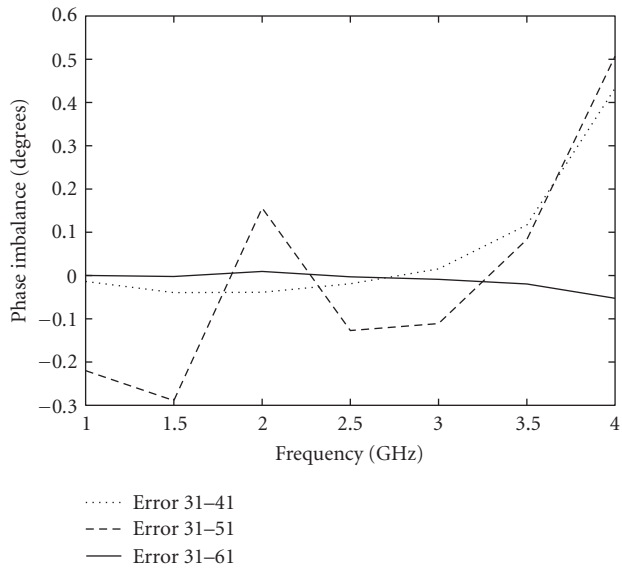FIGURE 12: The theoretically predicted response of the ideal 2×2 coupler.

FIGURE 13: The predicted phase imbalance of an ideal 2×2 coupler.

FIGURE 14: The predicted amplitude imbalance of an ideal 2×2 coupler.
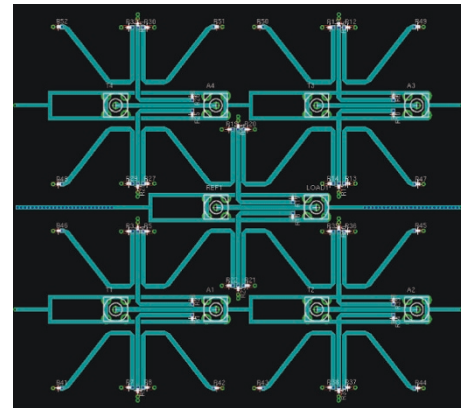
FIGURE 15: The PCB layout of the centre stripline controlled impedance conductor layer.

A,D (X,Z) type error and an A,C (X,Y) type error. This has the overall effect of reducing error. Were there to be a diagonal bias toward the distribution of error, then the error would accumulate.

Also visible in these results is a greater phase and amplitude balance between the symmetrically identical coupler pairs. For example, the phase and amplitude imbalance between ports 3 and 6 is very high. This leads to efforts to increase symmetry in the design, particularly the grounding via screens.

4.3. Measured coupler performance

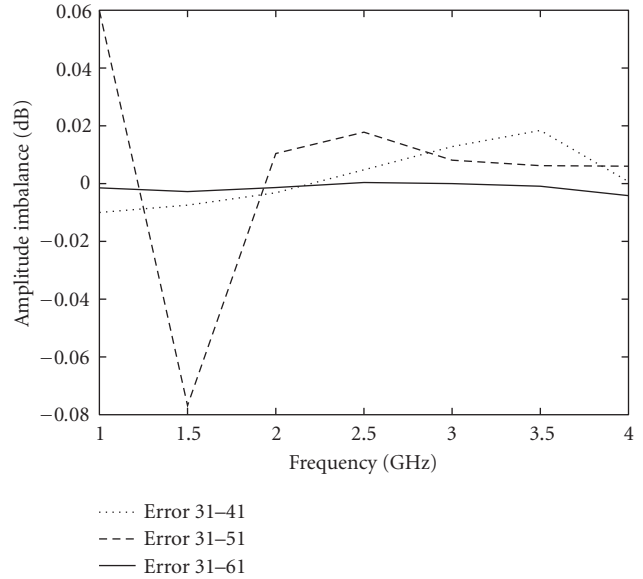Our design for Figure 11 was manufactured on a low-cost FR-4 substrate using a stripline design produced in Eagle [20]—see Figure 15. Additional grounding strips, connected by blind vias to the top and bottom ground layers, are visible which provide isolation between the individual couplers. A photograph of the finished 2×2 coupler manufactured by ECS circuits [21] is shown in Figure 16. Each of the coupler arms is terminated in low-quality surface mount $47\,\Omega$ resistors.

The 2×2 coupler was then tested using an R&S ZVB20 vector network analyser [22]. The results of this measurement with an input power of 0 dBm and 100 kHz of resolution bandwidth are shown in Figure 17. The coupler insertion loss is marginally higher than the theoretical prediction at 1.2 dB. This will affect the noise performance of the receiver and the transmit efficiency and hence must be budgeted for in our tower-top transceiver design. The
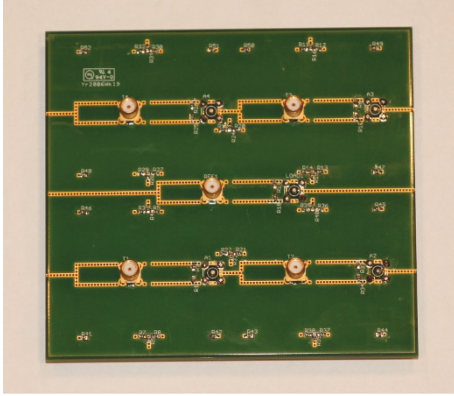
FIGURE 16: A photograph of the transceiver side of the calibration coupler board. The opposite side connects to the antenna array and acts as the ground plane.
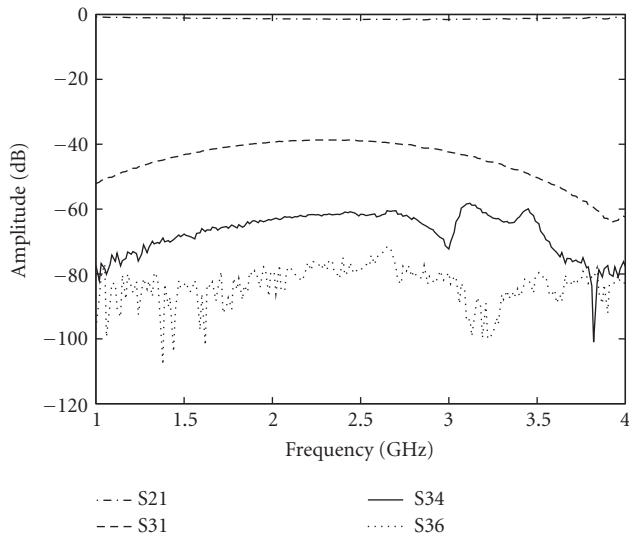

FIGURE 17: The measured performance of the prototype 2 × 2 coupler.

FIGURE 18: The measured phase imbalance of the 2 × 2 coupler.
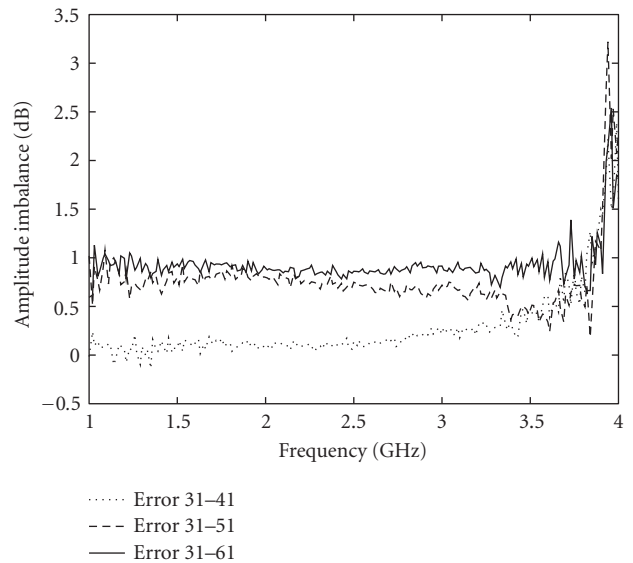
FIGURE 19: The measured amplitude imbalance of the 2 × 2 coupler.

coupled calibration path exhibits the desired coupling factor of −38.8 dB at our design frequency of 2.46 GHz. This stronger coupling, together with the finite loss tangent of our FR4 substrate, explain the increased insertion loss. The measured inter-transceiver isolation was measured at a minimum of −60.9 dB—thus the dominant source of (neighboring) inter-element coupling is likely to be antenna mutual coupling.

The other important characteristics of the coupler, its phase and amplitude balance, are shown in Figures 18 and 19 respectively. Phase balance is significantly poorer than indicated by the theoretical value. The maximum phase error recorded at our design frequency of 2.46 GHz for this coupler is 0.938°—almost an order of magnitude worse than the predicted imbalance shown in Figure 13.
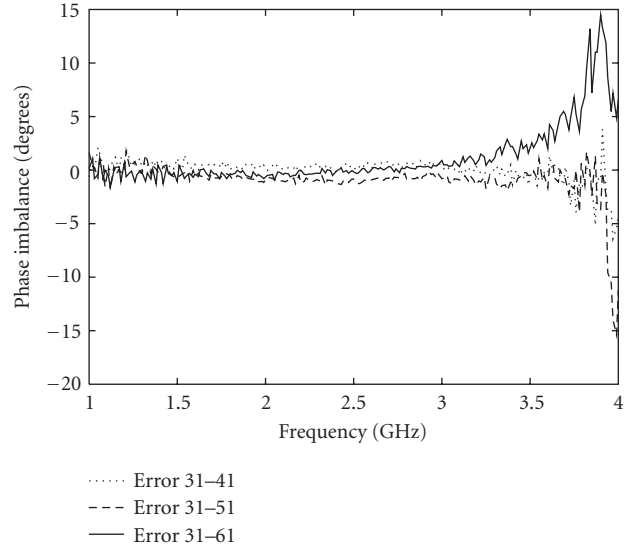
The amplitude balance results, Figure 19, are similarly inferior to the ADS predictions (contrast with Figure 14). The greatest amplitude imbalance is between S31 and S61 of 0.78 dB—compared with 0.18 dB in simulation. However, clearly visible in the amplitude response, and hidden in the phase error response, is the grouping of error characteristics between the paths S31-S41 and S51-S61.

Because the coupler error did not cancel as predicted by the ADS simulation, but is closer in performance to the series connection of a pair of individual couplers, future simulation of the calibration coupler should include Monte Carlo analysis based upon fabrication tolerance to improve the accuracy of phase and amplitude balance predictions.

Clearly a single coupler board cannot be used to characterise all couplers. To improve the statistical relevance of our
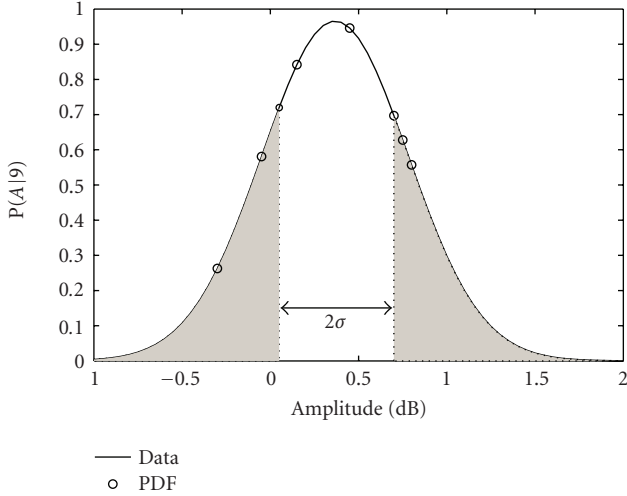
FIGURE 20: The measured coupler amplitude imbalance fitted a Gaussian probability density function, $\sigma_A = 0.4131$ dB, $\mu_A = 0.366$ dB.
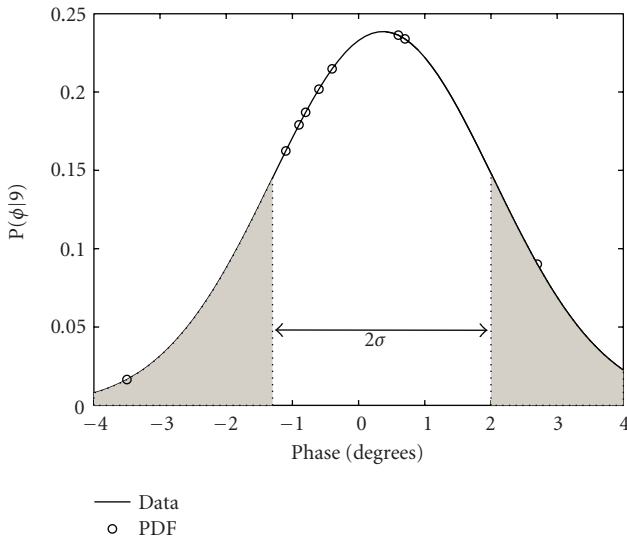

FIGURE 21: The measured coupler phase imbalance fitted to a Gaussian probability density function $\sigma_\phi = 1.672°$, $\mu_\phi = 0.371°$.
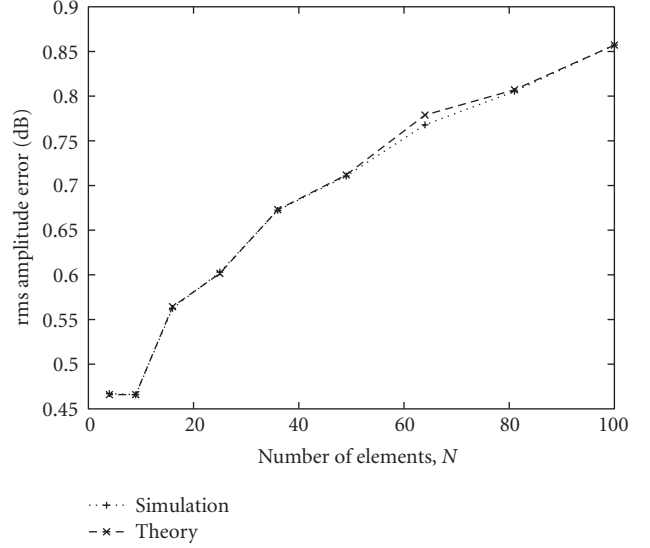

FIGURE 22: The theoretical prediction of overall array amplitude calibration accuracy based upon the use of the coupler hardware of Section 4.1.
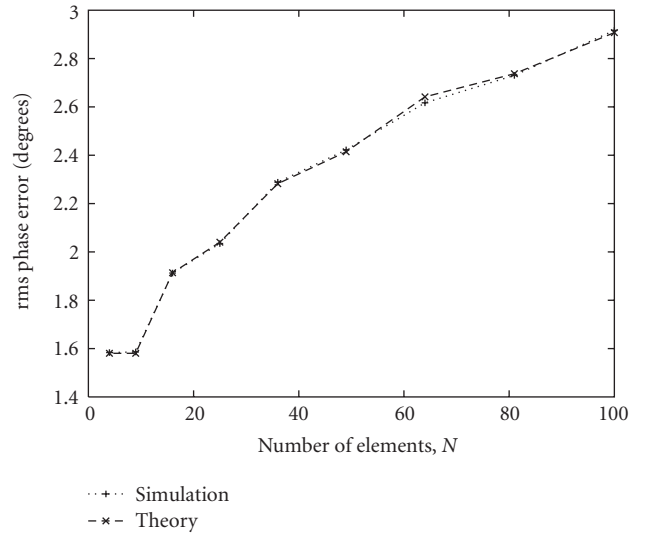

FIGURE 23: The theoretical prediction of overall array phase calibration accuracy based upon the use of the coupler hardware of Section 4.1.

results, three 2×2 coupler boards were manufactured and the phase and amplitude balance of each of them recorded at our design frequency of 2.46 GHz. These results are plotted against the Gaussian distribution to which the results were fitted for the amplitude and phase (Figures 20 and 21 correspondingly). Whilst not formed from a statistically significant sample (only nine points were available for each distribution), these results are perhaps representative of the calibration path imbalance in a small array. The mean and standard deviation of the coupler amplitude imbalance distribution are $\mu_{c_A} = 0.366$ dB and $\sigma_{c_A} = 0.4131$ dB. This error is somewhat higher than predicted by our theoretical study. Work toward improved amplitude balance is ongoing. The phase balance, with an rms error of $1.672°$, is of the order anticipated given the performance of the individual coupler.

With this additional insight into the statistical distribution of error for a single coupled calibration path, we may make inferences about the overall array calibration accuracy possible with such a system.

4.4. Predicted array calibration performance

To investigate the utility, or otherwise, of our practical array calibration system, the coupler statistics derived from our hardware measurements were fed into both the centre-referenced calibration algorithm simulation and the theoretical prediction of Section 3. The results of this simulation are shown in Figures 22 and 23.
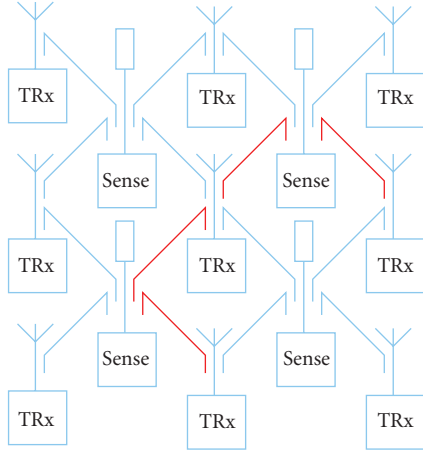
FIGURE 24: The redundant coupled calibration paths which may be useful in enhancing the quality of calibration.

The results from these figures show that the approach yields a highly accurate calibration, with rms phase errors for a typical 16-element array of less than 2° and a gain imbalance of less than 0.55 dB. As arrays increase in size, the errors do increase. For phase calibration, the increase is small even for very large arrays. Gain calibration is more sensitive to size and a 96-element array would have a 0.85 dB rms error. Ongoing work is focused upon improving the gain calibration performance for larger arrays. The following section is presenting some initial results for alternative calibration schemes which utilise the additional information from the redundant calibration paths.

5. FUTURE WORK

5.1. Redundant coupler paths

In each of the calibration algorithms discussed thus far, only a fraction of the available coupled calibration paths is employed. Figure 24 shows the coupled paths which are redundant in the "top-left" calibration scheme of Figure 6(b). The focus of future work will be to exploit the extra information which can be obtained from these redundant coupler paths.

5.2. Iterative technique

5.2.1. Operation

Given that we cannot measure the array output without incurring error due to the imbalance of each coupler, we have devised a heuristic method for enhancing the antenna array calibration accuracy. This method is designed to exploit the additional, unused coupler paths and information about the general distribution and component tolerance of the errors within the calibration system, to improve calibration accuracy. One candidate technique is based loosely on the iterative algorithmic processes outlined in [23]. Our method is a heuristic, threshold-based algorithm and attempts to infer the actual error in each component of the calibration system—allowing them to be compensated for.
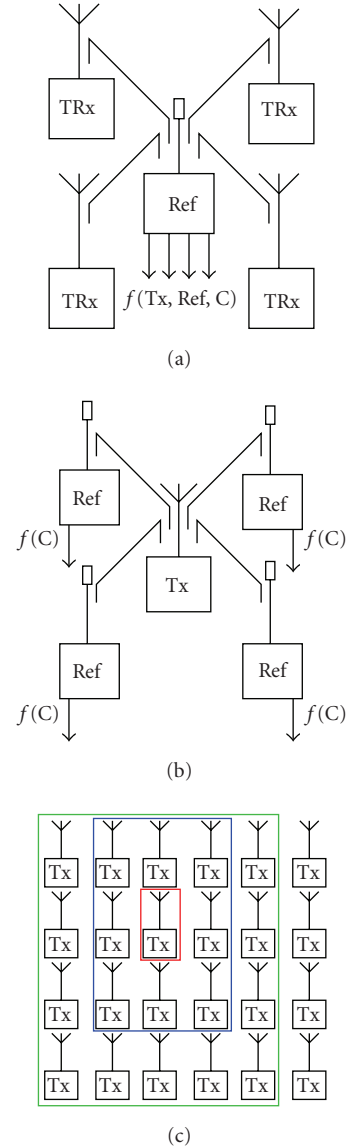

FIGURE 25: The two main processes of our heuristic method: (a) reference characterisation and (b) transmitter characterisation. (c) The error dependency spreads from the neighbouring elements with each iteration of the heuristic process.

Figure 25 illustrates the two main processes of our iterative heuristic algorithm. The first stage, Figure 25(a), is the measurement of each of the transmitters by the reference elements connected to them. The output of these measurements, for each reference, then have the mean performance of each neighbouring measured blocks subtracted. This results in four error measurements (per reference element) that are a function of the proximate coupler, reference and transmitter errors. Any error measurements which are greater than one standard deviation from the mean transmitter and coupler output are discarded. The remaining error measurements, without the outliers, are averaged and are used to estimate the reference element error.

The second phase, Figure 25(b), repeats the process described above, this time for each transmitter. Here the functionally equivalent step of measuring each transmitter by the four neighbouring references is performed. Again, the mean performance of each block in the signal path is calculated and subtracted. However, during this phase the reference error is treated as a *known* quantity—using the inferred value from the previous measurement. Based on this assumption, the resultant error signal is a function of the coupler error and the common transceiver element alone.

By extrapolating the transmitter error, using the same process as for the reference element, the coupler errors may be calculated and compensated for by weighting the transceiver input. This process is repeated. In each subsequent iteration, the dependency of the weighting error signal is dependent upon successive concentric array elements as illustrated in Figure 25(c).

The iterative process continues for much greater than n iterations, until either subsequent corrective weightings are within a predefined accuracy, or until a time limit is reached.

Cognisant of the negative effect that the peripheral elements of the array will have on the outcome of this calibration scheme, these results are discarded. For the results presented here, this corresponds to the connection of an additional ring of peripheral reference elements to the array. Future work will focus on the combining algorithmic and conventional calibration techniques to negate the need for this additional hardware.

5.2.2. Provisional results

To test the performance of this calibration procedure, the results are of 1000 simulations of a 10×10 array, each performed for 100 calibration iterations, was simulated using the system settings of Section 4.4. The centre calibration scheme gave an overall rms array calibration accuracy (σ_a) of 0.857 dB and 2.91°. The iterative calibration procedure gives a resultant phase accuracy of 1.32° and amplitude accuracy of 0.7148 dB. Figure 26 shows how the amplitude accuracy of the iterative calibration varies with each successive iteration. The horizontal line indicates the performance of the centre-referenced calibration. A characteristic of the algorithm is its periodic convergence. This trait, shared by simulated annealing algorithms, prevents convergence to (false) local minima early in the calibration process. This, unfortunately, also limits the ultimate accuracy of the array calibration. For instance, the phase accuracy of this array (Figure 27) degrades by 0.1° to 1.32° from its minimum value, reached on the 37th iteration. Future work will focus on tuning the algorithm's performance, perhaps to attenuate this oscillation in later iterations with a temperature parameter (T) and associated reduction function $f(T)$. Hybrid algorithms—targeting different calibration techniques at different sections of the array—are also currently under investigation.

6. CONCLUSION

In this paper, we have presented a new scheme for tower-top array calibration, using a series of nonradiative, interlinear
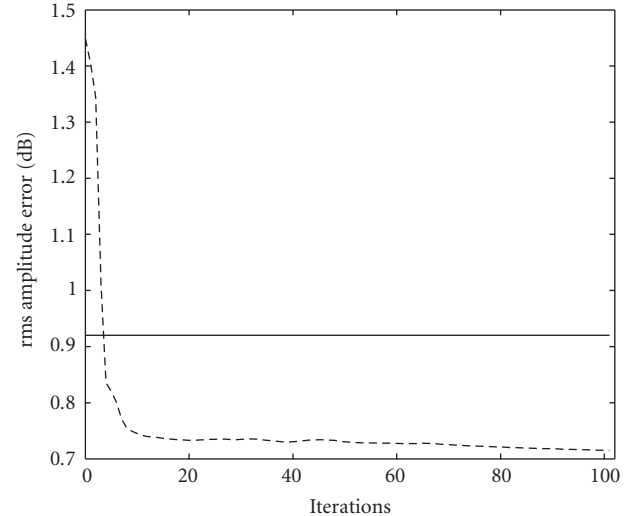

FIGURE 26: Resultant array amplitude feed-point calibration accuracy (σ_{a_A}) for a single $N = 100$ array, plotted versus the number of calibration iterations.
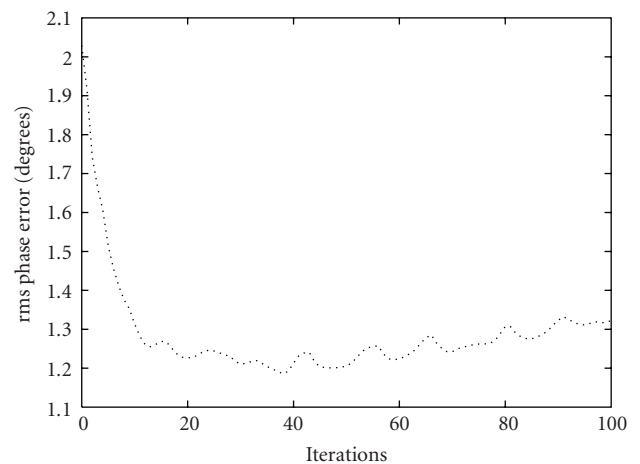

FIGURE 27: Resultant array phasing feed-point calibration accuracy (σ_{a_ϕ}) for a single $N = 100$ array, plotted versus the number of calibration iterations.

reference elements to sense the output of the array. The accuracy of this calibration scheme is a function of the array size, the calibration path taken in calibrating the array, and the coupler performance. Where the measurement accuracy is unlimited, then the accuracy of this calibration is dependent upon the number of couplers in a given calibration path.

The basic building block of this calibration scheme is the 2×2 array calibration coupler. We have shown that using low-cost fabrication techniques and low-quality FR-4 substrate, a broadband coupler network with rms phase balance of 1.1175° and amplitude balance of 0.3295 dB is realisable.

Based upon this coupler hardware, we have shown that phase calibration accurate enough for cellular smart antenna applications is possible. Although amplitude accuracy is still outside our initial target, work is ongoing on improving the

precision coupler network and on the development of calibration algorithms to further reduce this requirement.

Finally, we presented examples of one such algorithm—whose performance, unlike that of the conventional feedback algorithms, improves with array size. Moreover, this calibration algorithm, which is based upon exploiting randomness within the array, outperforms conventional calibration for large arrays. Future work will focus on use of simulated annealing and hybrid calibration algorithms to increase calibration accuracy.

ACKNOWLEDGMENT

REFERENCES

[1] N. Tyler, B. Allen, and H. Aghvami, "Adaptive antennas: the calibration problem," *IEEE Communications Magazine*, vol. 42, no. 12, pp. 114–122, 2004.

[2] C. M. Simmonds and M. A. Beach, "Downlink calibration requirements for the TSUNAMI (II) adaptive antenna testbed," in *Proceedings of the 9th IEEE International Symposium on Personal, Indoor and Mobile Radio Communications (PIMRC '98)*, vol. 3, pp. 1260–1264, Boston, Mass, USA, September 1998.

[3] K. Sakaguchi, K. Kuroda, J.-I. Takada, and K. Araki, "Comprehensive calibration for MIMO system," in *Proceedings of the 5th International Symposium on Wireless Personal Multimedia Communications (WPMC 3'02)*, vol. 2, pp. 440–443, Honolulu, Hawaii, USA, October 2002.

[4] C. M. S. See, "Sensor array calibration in the presence of mutual coupling and unknown sensor gains and phases," *Electronics Letters*, vol. 30, no. 5, pp. 373–374, 1994.

[5] R. Sorace, "Phased array calibration," *IEEE Transactions on Antennas and Propagation*, vol. 49, no. 4, pp. 517–525, 2001.

[6] K. R. Dandekar, L. Hao, and X. Guanghan, "Smart antenna array calibration procedure including amplitude and phase mismatch and mutual coupling effects," in *Proceedings of the IEEE International Conference on Personal Wireless Communications (ICPWC '00)*, pp. 293–297, Hyderabad, India, December 2000.

[7] T. Kaiser, "When will smart antennas be ready for the market? Part I," *IEEE Signal Processing Magazine*, vol. 22, no. 2, pp. 87–92, 2005.

[8] F. Rayal, "Why have smart antennas not yet gained traction with wireless network operators?" *IEEE Antennas and Propagation Magazine*, vol. 47, no. 6, pp. 124–126, 2005.

[9] G. Brown, "3G base station design and wireless network economics," *Unstrung Insider*, vol. 5, no. 10, pp. 1–30, 2006.

[10] J. D. Fredrick, Y. Wang, and T. Itoh, "A smart antenna receiver array using a single RF channel and digital beamforming," *IEEE Transactions on Microwave Theory and Techniques*, vol. 50, no. 12, pp. 3052–3058, 2002.

[11] S. Ishii, A. Hoshikuki, and R. Kohno, "Space hopping scheme under short range Rician multipath fading environment," in *Proceedings of the 52nd Vehicular Technology Conference (VTC '00)*, vol. 1, pp. 99–104, Boston, Mass, USA, September 2000.

[12] A. J. Cooper, "'Fibre/radio' for the provision of cordless/mobile telephony services in the access network," *Electronics Letters*, vol. 26, no. 24, pp. 2054–2056, 1990.

[13] G. Brown, "Open basestation bonanza," *Unstrung Insider*, vol. 4, no. 7, pp. 1–20, 2005.

[14] T. Cooper and R. Farrell, "Value-chain engineering of a tower-top cellular base station system," in *Proceedings of the IEEE 65th Vehicular Technology Conference (VTC '07)*, pp. 3184–3188, Dublin, Ireland, April 2007.

[15] T. S. Cooper, R. Farrell, and G. Baldwin, "Array Calibration," Patent Pending S2006/0482.

[16] T. Cooper, J. McCormack, R. Farrell, and G. Baldwin, "Toward scalable, automated tower-top phased array calibration," in *Proceedings of the IEEE 65th Vehicular Technology Conference (VTC '07)*, pp. 362–366, Dublin, Ireland, April 2007.

[17] Analog Devices Datasheet, "400 MSPS 14-Bit DAC 1.8V CMOS Direct Digital Synthesizer," January 2003.

[18] T. S. Cooper, G. Baldwin, and R. Farrell, "Six-port precision directional coupler," *Electronics Letters*, vol. 42, no. 21, pp. 1232–1234, 2006.

[19] Agilent EEsof, Palo Alto, Calif, USA. Advanced Design System, Momentum.

[20] CadSoft Computer, 801 South Federal Hwy., Suite 201, Delray Beach, FL 33483-5185. Eagle.

[21] ECS Circuits, Unit 2, Western Business Park, Oak Close, Dublin 12, Ireland.

[22] Rhode & Schwartz Vertiriebs-GmbH, Muehldorfstrasse 15, 81671 Muenchen, Germany.

[23] J. Hromkovic, *Algorithmics for Hard Problems*, Springer, Berlin, Germany, 2nd edition, 2004.